




Engineering pyridinic and pyrrolic N-enriched graphene quantum dots to strengthen metal-support interactions for highly efficient methanol oxidation

Ye Fan¹, Chenyao Hu², Wenyao Zhang^{1,*} , Yongsheng Fu^{1,*}, and Xin Wang¹

¹Key Laboratory of Soft Chemistry and Functional Materials, Nanjing University of Science and Technology, Ministry of Education, Nanjing 210094, China

²Testing and Analysis Center, Nanjing Forestry University, Nanjing 210037, China

Received: 24 August 2021

Accepted: 28 December 2021

Published online:
20 January 2022

© The Author(s), under exclusive licence to Springer Science+Business Media, LLC, part of Springer Nature 2022

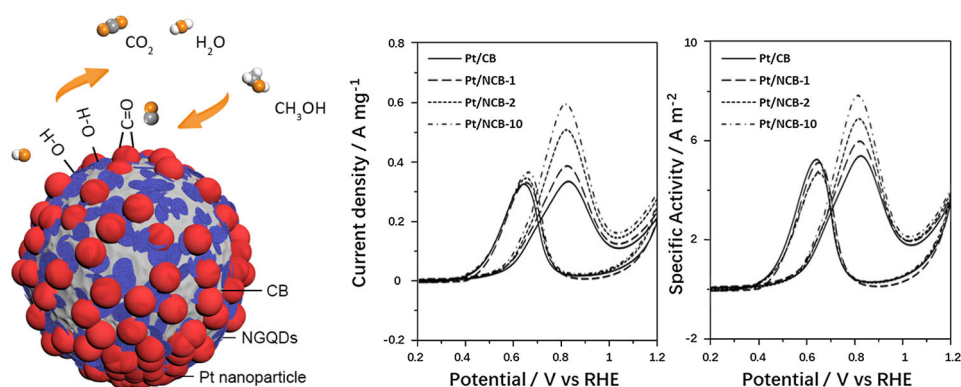
ABSTRACT

Structural engineering carbon support in controlling the dopant concentrations or types and their homogeneity is an effective way to modulate the catalytic properties of Pt-based materials. Herein, we reported a convenient and scalable strategy to incorporate pyridinic and pyrrolic N components into the carbon matrix via quantum dots anchoring pathway. The newly designed carbon can accurately regulate the N contents, and importantly, exposes numerous functional edge sites for growing and stabilizing Pt nanoparticles with a very narrow size distribution. Experimental validation identified that a strengthened metal-support interaction is afforded on this Pt/NCB-*n* architecture, which significantly optimizes its catalytic behaviors toward the methanol electrooxidation process. Combining its unique textural features including unimpeded electron conductivity, intensive N components on the triple-phase boundaries, and sufficient accessible catalytically active centers, the obtained Pt/NCB-*n* exhibits a marvelous electrocatalytic activity accompanied by distinguished anti-poisoning ability and reliable long-term stability, holding great potential as substitutes for conventional Pt-activated carbon catalysts. This study paves a new avenue to develop more effective carbon-based supports for constructing advanced electrocatalysts and can also be extended to the next-generation metal-air batteries, metal-ion batteries, or sensors.

Handling Editor: Andrea de Camargo.

Address correspondence to E-mail: zhang-wenyao@163.com; fuyongsheng0925@163.com; fuyongsheng@njust.edu.cn

GRAPHICAL ABSTRACT



Introduction

The continuous consumption of fossil fuels and the accompanying global warming issues triggers the development of highly efficient energy storage and conversion technologies [1–3]. Among the various candidates, direct alcohol fuel cells (DAFCs) attract increasing attention because of their high energy conversion efficiency, low costs and convenient storage of the fuels, zero pollutant emission, as well as facile power-system integration [4, 5]. In particular, the performance of the DAFCs, including energy densities and the lifespans, depends primarily on the electrocatalytic properties of the electrode materials, [6, 7] which motivates great endeavors on the exploration of highly active and stable electrocatalysts.

Platinum (Pt) is the well-known most effective electrocatalyst, however, the low natural abundance and the limited mined amount each year make the Pt an extremely high cost, which greatly limits their large-scale commercial application [8–10]. Some Pt-free oxygen reduction reaction catalysts have been intensively studied, including, cheaper noble metal catalysts (Palladium [11, 12], Iridium [13], Ruthenium [14], Silver [15]), non-precious metal catalysts (transition metal–nitrogen–carbon (M–N–C) complexes [9, 16–19], Manganese perovskite [20, 21]) and metal-free catalysts (heteroatoms-doped graphene [6, 22],

ordered mesoporous carbon [23, 24]). They deliver high activities and potentials to replace the Pt-based cathode but for the anodic catalytic reactions, it still relies on the Pt-based materials. Therefore, minimizing the amount of platinum and improving its catalytic activity and stability for anodic catalysis in DAFCs has long been a hot topic of research. According to the current study, there are three main strategies to enhance the performance of Pt-based catalysts, (1) optimizing the Pt-based catalyst preparation methodology: employing different reducing agents, protecting agents or reaction conditions to synthesize Pt nanoparticles with unique morphologies to improve the Pt utilization efficiency, thus enhancing its electrocatalytic activity; [25–28] (2) engineering the microstructure of Pt-based catalysts, such as fabricating Pt-based bimetallic or multi-metallic catalysts [29–31], forming Pt-based alloys [27, 32, 33], constructing core-shells [34–36], heterojunctions structures [37, 38], aiming to strengthen the reaction kinetics and the poison tolerance through bifunctional mechanisms and synergistic effects; (3) integrating the Pt-based catalyst with functional substrates to anchor and stabilize the highly mobile Pt nanoparticles, and accordingly modulate their reactivities. [39–41]

Immobilizing the Pt nanoparticles onto conductive carbon-based supports including carbon black, carbon fibers, carbon nanotubes, and graphene, is considered as one of the most direct and effective ways

to localize the Pt nanoparticles on a specific site, simultaneously downsize the nanoparticles, and control the morphologies. [42, 43] Most recently, the development of the heteroatom doping technique on carbon opens up new avenues for high-performance electrocatalysts, which have just experienced a renaissance. [44–46] The extensive theoretical and experimental evaluation identified that the substituted N atoms are capable of manipulating the spin density and the charge distribution of neighboring carbon atoms, hence remarkably improving the chemical inertness of the pristine carbon supports. [47] On the other hand, the electron lone pairs upon N atoms can insistently capture metal ions in the solution and enormously strengthen the supports' affinity for anchoring metal nanoclusters. [48, 49] This strong electronic interaction plays a crucial role in tethering Pt nanoparticles and avoiding them from dissolving, migrating, and agglomerating during the catalytic reactions. [40] Importantly, it can also modulate the d-band center and the Fermi level of the Pt nanoparticles, which promotes the intermediates desorption and accelerates the catalytic process. [50] Among various substituted N species, the pyridinic and pyrrolic N are regarded as the main components in anchoring the metal particles and maximizing the above merits. [51] However, conventional N-doping approaches, for instance, chemical vapor deposition, plasma treatment, or thermal treatment, lead to complex N configurations and reduced conductivity, thus it still remains a big challenge to incorporate N into carbons with a high proportion of desired certain N configuration and acceptable electric conductivity.

In this work, we report a facile strategy for large-scale production of N-doped graphene quantum dots (NGQDs) decorated carbon supports, which achieves incorporating N in rich of highly active pyridinic and pyrrolic N configurations. This newly designed carbon support then acts as a platform to stabilize narrowly distributed, uniformly dispersed, and nanometric Pt nanoparticles towards methanol oxidation in DAFCs. The surface integrating NGQDs realizes accurately controlling the doping concentration and localizes the functional N components on the triple-phase boundaries, which ensures rapid electron transfer in the intrinsic structure of carbon, and involves numerous edge planes for Pt nucleation and electrolyte diffusion, as well as enhances the interactions between Pt and the carbon. Consequently, the Pt/NCBs exhibit meritorious

electrocatalytic performance in terms of large electrochemically active surface areas, high forward peak current densities, unusual poison tolerances, and reliable long-term stabilities, superior to the commercial Pt-activated carbon catalysts.

Experimental section

Preparation of Pt/NCB catalysts

The Graphite oxide was prepared from natural flake graphite powder according to Hummer's method. [52, 53] The NGQDs were synthesized by a combined chemical etching and hydrothermal process. In a typical procedure, 1.0 g freeze-dried graphite oxide was put into an aqueous mixture containing 20 mL concentrated sulfuric acid and 20 mL concentrated nitric acid followed by ultrasonication for 2 h and refluxing at 90 °C for 6 h. After cooling to room temperature, the suspension was centrifuged for 10 min. The supernatant was collected and neutralized by adding sodium hydroxide solution, then dialyzed against pure water for 2 weeks in a 500 Da molecular weight cut-off dialysis bag. The resulting graphene quantum dots (GQDs) were freeze-dried and labeled as GQDs. Next, 10 mg GQDs was dispersed in 100 mL dimethylformamide (DMF) under ultrasonication. The reaction mixture was transferred into a Teflon-lined stainless steel autoclave for hydrothermal treatment at 200 °C for 24 h. Afterward, the rotary evaporator was applied to remove the solvent, and the as-synthesized product, labeled as NGQDs, was washed, dialyzed, and finally freeze-dried. As to deposit NGQDs onto the carbon support, 100 mg Vulcan XC-72 carbon black (labeled as CB, Cabot Corporation) with various amounts (1, 2, 10 mg) of NGQDs were suspended in 200 mL water followed by ultrasonication for 2 h. After filtrated and freeze-dried, the N-doped carbon support was obtained and labeled as NCB-*n*, where *n* represents the starting amount of NGQDs.

Subsequently, the Pt nanoparticles were grown and stabilized onto the NCB-*n* supports. Typically, 120 mg NCB-*n* was added into 240 mL ethylene glycol solution (0.5 mg mL⁻¹) and ultrasonicated by 1 h to form a stable dispersion. Afterward, 0.167 mL of 0.94 M K₂PtCl₄ solution (Alfa Aesar) was slowly dropped in with magnetic stirring. The reaction mixture was then refluxed at 120 °C for 16 h, during

which the Pt^{2+} ions were reduced by the ethylene glycol via a solvothermal strategy [54], followed by centrifuged, washed, and finally freeze-dried. The product was denoted as Pt/NCB-*n*. For comparison, Pt nanoparticles supported on pristine carbon black were also prepared by a similar procedure and denoted as Pt/CB. The actual platinum loadings of Pt/NCB-1, Pt/NCB-2, Pt/NCB-10, and Pt/CB confirmed by inductively coupled plasma atomic emission spectrometry (ICP-AES, Varian Vista-AX) analysis were 19.1, 19.7, 19.2, and 19.2 wt%, close to the theoretical value of 20.0 wt%.

Characterization

Field-emission scanning electron microscopy (FE-SEM, JEOL JEM7800F) equipped with energy-dispersive X-ray spectroscopy (EDX) and Transmission electron microscopy (TEM, JEOL JEM-2100) were employed to investigate the morphology of the samples. X-ray photoelectron spectra (XPS) were performed using a Thermo-VG Scientific ESCALAB 250 X system. Powder X-ray diffraction (XRD) patterns were recorded on a Bruker D8 Advance diffractometer with Cu $K\alpha$ radiation. Fourier Transform-IR spectra (FT-IR) were obtained on a Nicolet iS20 instrument (Thermo Nicolet Corporation). UV-Vis absorption spectra were collected with a SHIMADZU TU-1800 UV-Visible-NIR spectrometer. Fluorescence emission spectroscopy was carried out on an LS-45 fluorescence spectrophotometer (Perkin Elmer, UK). The metal loadings of the samples were determined by a Varian Vista-AX ICP-AES.

Electrochemical measurements

All electrochemical experiments were performed in a CHI 760E electrochemical workstation using a standard three-electrode configuration, which consisted of a glass carbon (GC) disk coated with catalysts serving as the working electrode, a saturated calomel electrode (SCE) serving as the reference electrode, a Pt wire serving as the counter electrode. The working electrode was prepared as follows: 2 mg of the catalyst was dispersed in a mixed solution (0.667 mL water, 0.333 mL isopropyl alcohol, 50 μL 5% Nafion 117 solution) under the assistance of ultrasonic treatment to form a homogeneous black ink. 5 μL of the resulting ink was carefully pipetted on the well-polished GC electrode surface and dried in the air

before measurements. The electrochemically active surface area (ECSA) values of the catalysts were evaluated by both hydrogen and CO adsorption/desorption cyclic voltammogram (CV) curves in 0.5 M H_2SO_4 electrolyte. The methanol electrooxidation performance of the catalysts was recorded in N_2 -saturated 1 M CH_3OH and 0.5 M H_2SO_4 electrolyte and 1 M CH_3OH and 1 M NaOH electrolyte. All the electrochemical data were normalized to the mass of Pt. The potentials in this work were expressed with the reversible hydrogen electrode (RHE) by calibrating the SCE to the RHE scale.

Results and discussion

Firstly, the morphology of the as-prepared graphene-based quantum dots was characterized by TEM. As illustrated in Fig. 1a and b, both the GQDs and NGQDs are well monodispersed and homogeneous in size. Close inspection reveals a high crystallinity with a lattice fringe of 0.20 nm, assigning to the (102) diffraction planes of graphitic sp^2 carbon. A narrower distribution and smaller size can be noticed for NGQDs, implying that the peripheral defect sites and functional groups of GQDs were etched under the DMF hydrothermal treatment, thus reducing the particle size of quantum dots. XPS and FT-IR analysis were employed to evaluate the chemical structure and composition of the graphene-based quantum dots. The XPS survey scan spectra of GQDs and NGQDs in Figure S1 discloses that the as-obtained quantum dots are composed of C, N, and O elements without any obvious impurity. The high-resolution $\text{C}1\text{s}$ XPS spectrum of GQDs can be deconvoluted into three peaks centered at 284.6, 286.3, and 288.9 eV (Fig. 1c), which are corresponded to graphitic $\text{C}=\text{C}$, $\text{C}-\text{OH}$, and $\text{C}=\text{O}$ groups, respectively. [40, 47] It should be noted that the high proportion of oxygen-containing groups was involved by the Hummer's oxidation and ensured the extraordinary dispersion ability and stability of GQDs in the solvent, matching well with the previously reported carbon-based quantum dots. [55, 56] The contents of $\text{C}-\text{OH}$ and $\text{C}=\text{O}$ groups decreased distinctly in that of NGQDs, and two additional peaks were located at 285.6 eV (sp^2 $\text{C}=\text{N}$) and 287.3 eV (sp^3 $\text{C}-\text{N}$) were raised. This gave strong evidence of the incorporation of N atoms in the framework of graphene quantum dots, which was further supported by the FT-IR spectrum of the

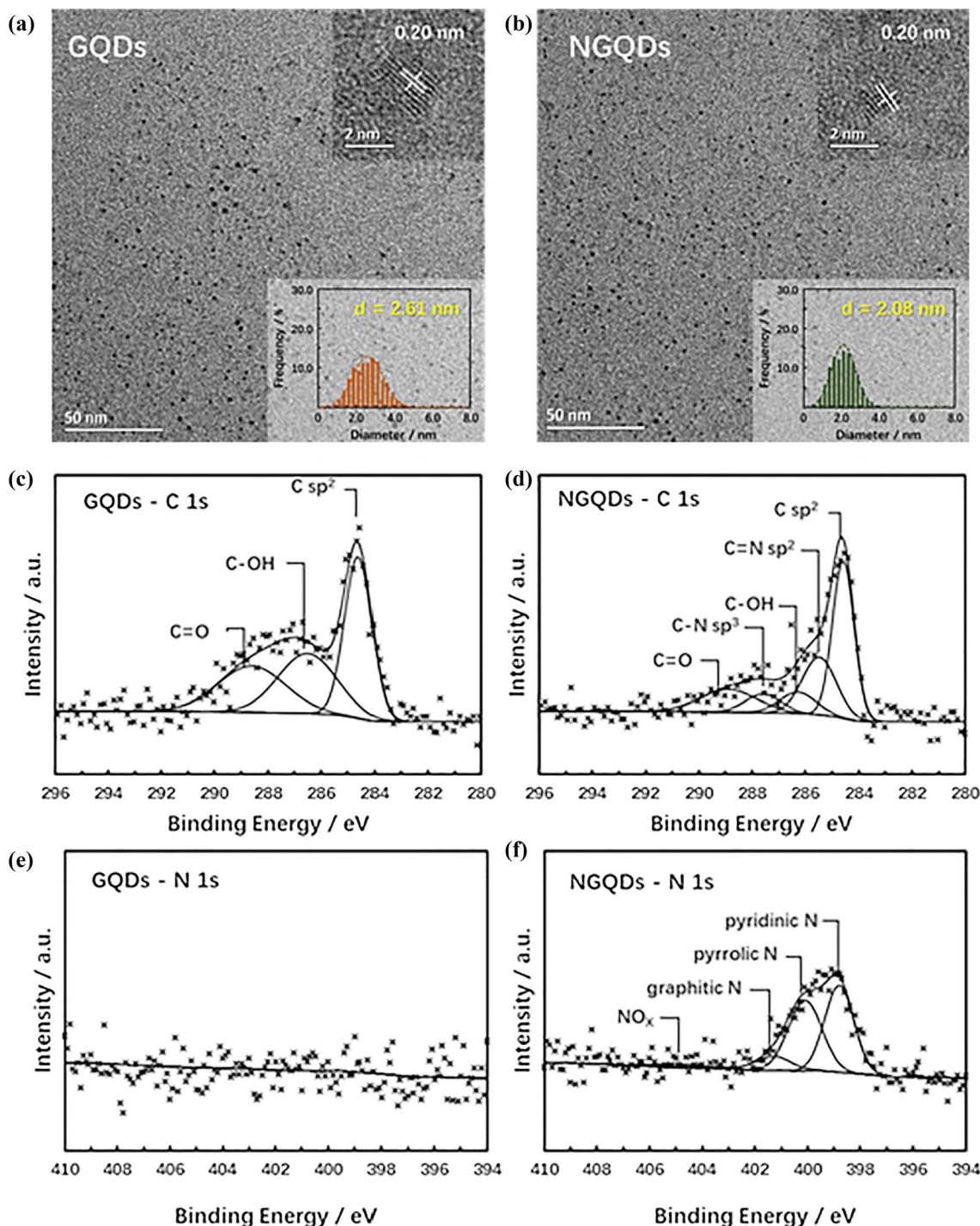


Figure 1 Morphological and structural analysis of the as-prepared carbon-based quantum dots. TEM images of (a) GQDs and (b) NGQDs, inserts are the corresponding HRTEM image and the

characteristic C=N stretching vibration at 1420 and 1240 cm^{-1} [57] for NGQDs in Figure S2. Meanwhile, Fig. 1e and f showed the high-resolution N 1s spectra of GQDs and NGQDs. No evident single can

be found in that of GQDs, whereas four components can be distinguished in that of NGQDs, that is pyridinic, pyrrolic, graphitic, and oxidized nitrogen, respectively. Importantly, over 90% of the nitrogen

atoms are involved in the form of pyridinic and pyrrolic configuration, which played extremely critical roles in stabilizing Pt nanoparticles during the synthesis and catalytic procedures and it will be discussed in the following sections.

The optical properties of the GQDs and NGQDs were then evaluated by UV-Vis absorption and fluorescent spectroscopy. As shown in Figure S3a, The GQDs possessed a well-defined absorption band at 223 nm, attributed to the π - π^* transition of the aromatic sp^2 bonds. [58, 59] The symmetrical fluorescence spectra revealed that the emission peak is 438 nm at the excitation wavelength of 370 nm. Taking quinoline sulfate as a standard, the fluorescence quantum yield of the GQDs can be calculated as 12.5% at 370 nm, deriving from the area of the fluorescence emission peak and its corresponding absorption intensity (Figure S3b). In contrast, the absorption band of NGQDs presented an obvious red-shift (Figure S3c), indicating that the conjugated π structure in NGQDs has been modulated [60] and presumably a new surface state has been introduced by the nitrogen doping process. The emission peak of NGQDs appeared at 417 nm at the excitation wavelength of 360 nm, and the fluorescence quantum yield was demonstrated to be 14.4%, slightly higher than that of GQDs. Since the fluorescence quantum yield is related to the size of quantum dots [61–63], it can be confirmed that the size of GQDs was reduced after the hydrothermal doping process, as the above TEM observation, which also indicated that GQDs have been successfully modified by the nitrogen heteroatoms. These results were also supported by the excitation wavelength-dependent fluorescence behavior of both GQDs and NGQDs in Figure S4.

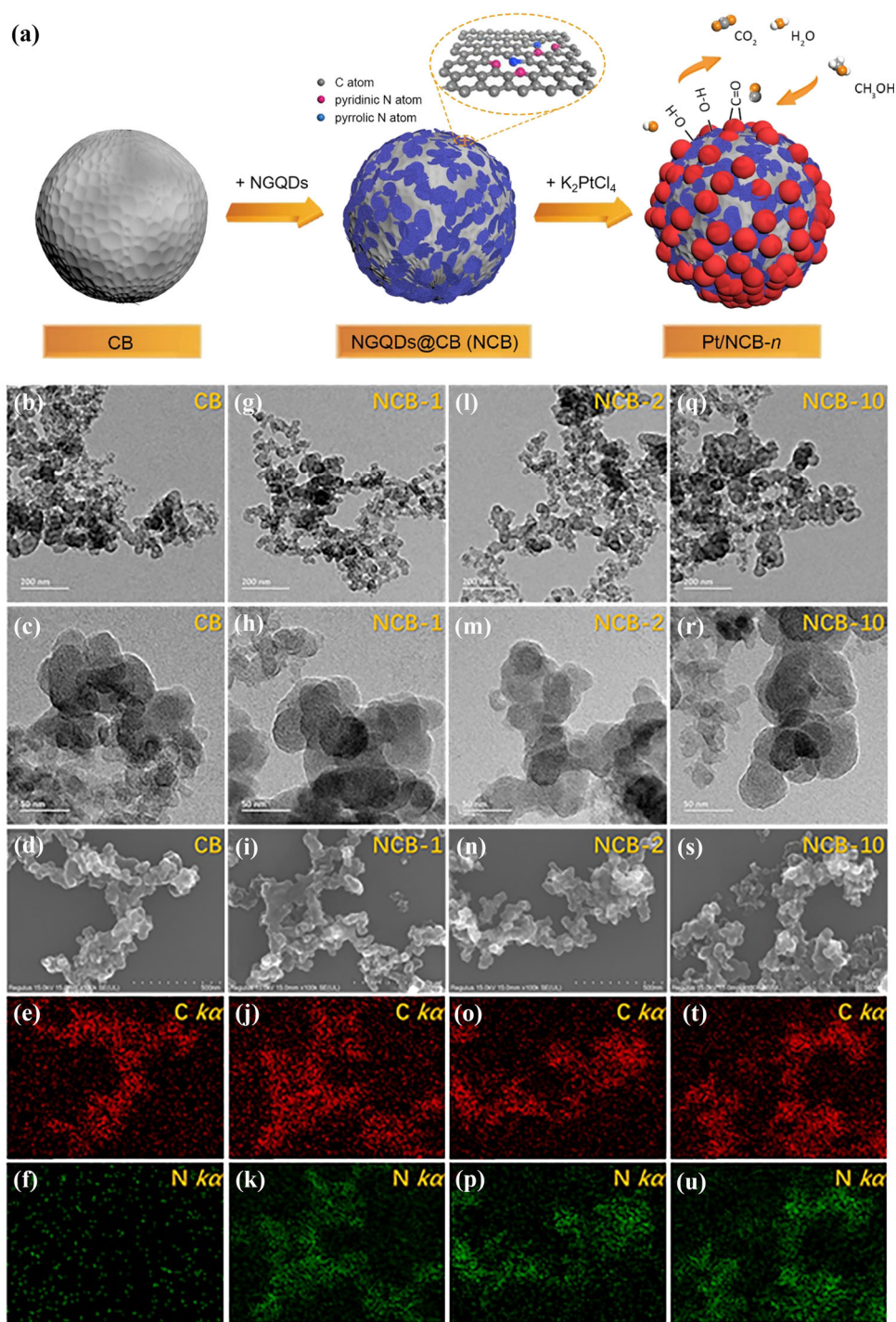
In the next set of experiment, the as-obtained NGQDs was ultrasonically deposited on conventional carbon black, aiming to chemically integrate the highly active nitrogen components on the carbon support (Fig. 2a). Various amount of NGQDs was considered and the saturated absorption is found to be NCB-10, detected by the UV-Vis technique on the filtrate after deposition, where the surface of CB is well-wrapped by NGQDs uniformly and densely. Either the pristine CB or NCB-*n* possessed a nanosphere morphology with a diameter of 20 ~ 100 nm (Fig. 2b–u) and a typical C (002) interplanar diffraction peak (Figure S5), suggesting no structural deterioration after depositing NGQDs. The corresponding EDX mapping then demonstrated the

incorporation of N element on CB, and the single of N increased linearly with the NGQDs deposition concentration. Another proof for this point was given by the XPS analysis (Figure S6). The evident N 1s response and the corresponding deconvoluted N components revealed the successful decoration of NGQDs on CB, that is, the resulting NCB-*n*. Subsequently, a soft chemistry methodology was used to load Pt nanoparticles on the NCB-*n* to testify our demonstrated highly active nitrogen configuration for anchoring small-sized Pt catalysts toward methanol electrooxidation.

TEM analysis in Fig. 3 clearly revealed the morphologies and the particle size distributions of the as-prepared Pt catalysts. For Pt/CB, Pt nanoparticles with an average diameter of 2.46 nm were dispersed on CB but several aggregates can be found, which may derive from a relatively weak interaction between Pt and the support. Closed TEM inspection exhibited an interplanar spacing of 0.23 nm, which correlates well with the typical lattice fringer of the Pt (111) crystal plane. [64] For Pt/NCB-*n*, it can be distinctly observed a more homogeneous dispersion along with a narrower size distribution, which originates from the strong coordination capacity of pyridinic and pyrrolic N components on NGQDs, thus effectively strengthening the interactions between the Pt and carbon support and evenly tethering Pt atoms during their nucleation and growth process. This phenomenon plays an important role in decreasing the probability of Ostwald ripening agglomeration during the methanol oxidation reactions. The Pt particle sizes were also found to be reduced with the NGQDs contents enhanced, indicating nitrogen components on CB are effectively conducive to the formation of smaller-sized Pt nanoparticles. Meanwhile, XRD results in Figure S7 showed the good crystallinity of the as-obtained Pt nanoparticles, and based on the Scherrer equation, the particle sizes are calculated, which is well consistent with the TEM results (Table S1).

To gain additional insight into the chemical states of the Pt/NCB-*n* catalysts, XPS measurement was carried out. As disclosed in Figure S8, the as-obtained Pt-based catalysts are composed of C, N, O, and Pt elements without any impurity, which suggests the successful reduction of Pt nanoparticles via the solvothermal approach. Figure 4 presented the high-resolution Pt 4f XPS spectra of Pt/CB, Pt/NCB-1, Pt/NCB-2, and Pt/NCB-10, respectively. The Pt 4f

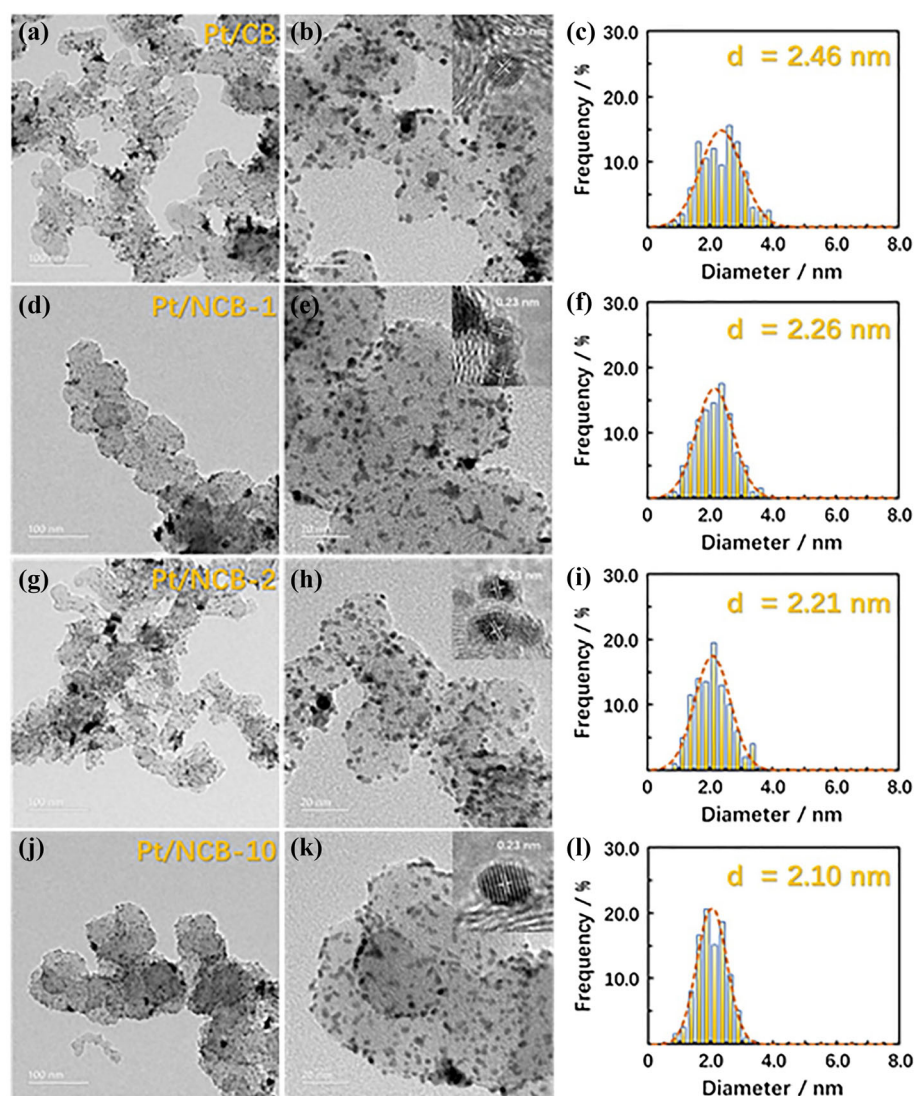
Figure 2 a Schematic of fabrication of Pt-NCB-*n* catalysts; Morphological analysis of the NGQDs modified carbon supports. Typical TEM images, FE-SEM images, and the corresponding C K α , N K α mapping images of (b–f) pristine carbon support, (g–k) NCB-1, (l–p) NCB-2, (q–u) NCB-10, respectively.



signals of these samples are similar in that all composed of two sets of peaks, the lower energy peaks located at ~ 70.8 eV and ~ 74.2 eV were ascribed to the zero-valence state of metallic Pt, the other shoulder peaks located at ~ 72.1 eV and ~ 75.4 eV belonged to the oxidation state of Pt (PtO_x) [65]. It should be noted that the binding energy of PtO_x

component in Pt/CB and all the Pt/NCB-*n* were more negative than that of pristine PtO. Combining that no diffraction peaks of platinum oxide were observed in the XRD patterns, it can be determined that these components owing to the oxygen-absorbing on part of platinum atoms on the surface of Pt nanoparticles. As listed in Table 1, the PtO_x

Figure 3 Morphological analysis of the Pt/NCB nanocomposite. Typical TEM images and the corresponding Pt particle size distribution of (a–c) Pt/CB, (d–f) Pt/NCB-1, (g–i) Pt/NCB-2, (j–l) Pt/NCB-10, respectively. Inserts are the corresponding HRTEM images.



contents increased in the order Pt/NCB-10 > Pt/NCB-2 > Pt/NCB-1 > Pt/CB, matching well with the average particle size obtained by TEM and XRD. This is derived from the fact of more exposed surface atoms on a smaller particle, which possess more active physicochemical behaviors. Additionally, with the increase of N contents in NCB, the peaks of Pt(0) shifted slightly to the low binding energy, indicating a reinforced metal-support interaction between the Pt nanoparticles and the NCB-*n* support, in favor of boosting the electrocatalytic stability toward methanol oxidation. Summarized from all the above structural characterization results, it is reasonable to deduce that a high active pyridinic and pyrrolic N are successfully integrated into the carbon support, which effectively reduces the particle size of Pt nanoparticles and optimizes their dispersion.

The electrochemically active specific surface area (ECSA) of the as-obtained Pt/NCB-*n* catalysts was firstly evaluated and compared with that of commercial used Pt/CB catalyst. Figure 5a showed the CV of these catalysts in the electrolyte of 0.5 M H₂SO₄ at a scan rate of 50 mV s⁻¹. It can be noted that these four catalysts presented a similar CV profile, which can be roughly divided into four regions. During the forward scan, the oxidation peaks at 0.05 ~ 0.30 V were assigned to the desorption of hydrogen (-H_{ads}) adsorbed on Pt catalysts. As the potential reached ~ 1.0 V, the surface Pt atoms were oxidized and adsorbed -OH_{ads} species. For the reverse scan, strong reduction peaks appeared at ~ 0.70 V ascribed to the desorption of -OH_{ads}, and the signals ~ 0.25 V belonged to the re-adsorption of -H_{ads}. Figure 5b exhibited a CO stripping voltammetry in

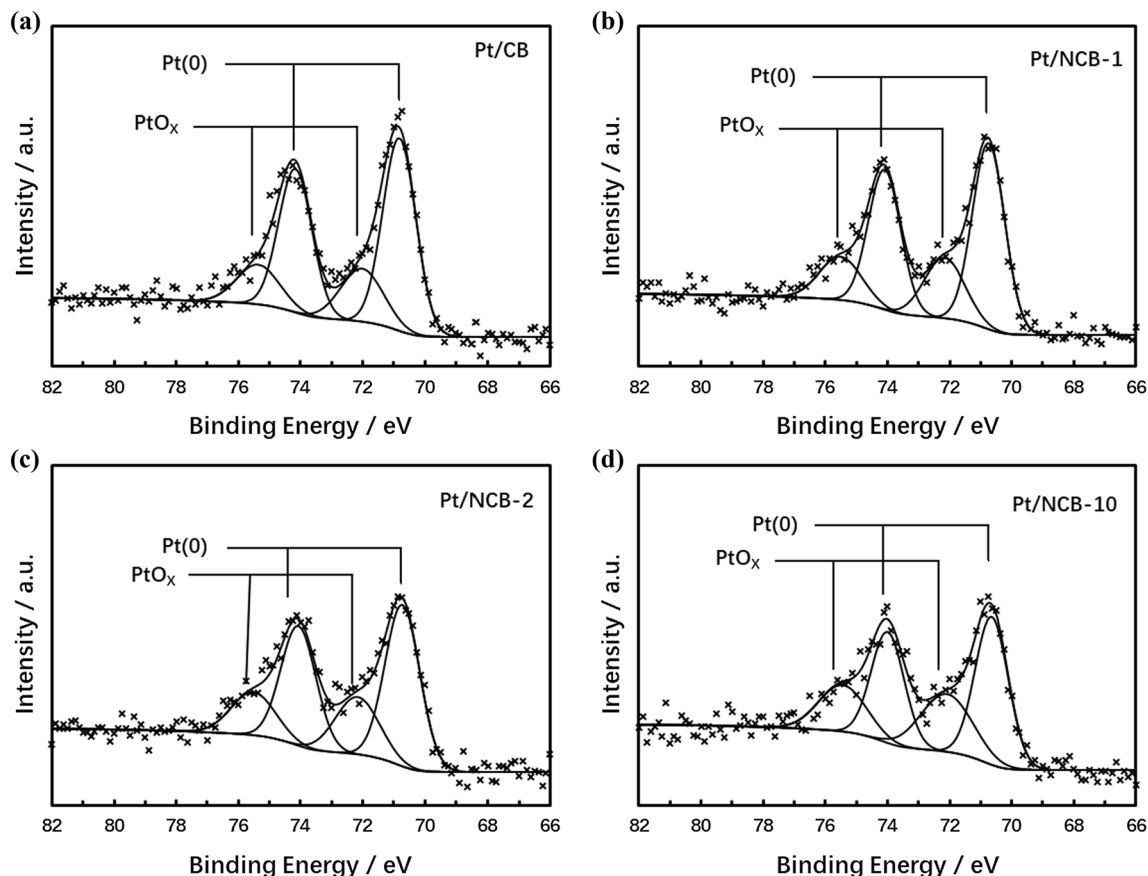


Figure 4 XPS analysis of the Pt/NCB nanocomposite. High-resolution Pt 4f XPS spectra of (a) Pt/CB, (b) Pt/NCB-1, (c) Pt/NCB-2, (d) Pt/NCB-10, respectively.

Table 1 Deconvolution data from Pt 4f XPS spectra of Pt/CB and Pt/NCB nanocomposites

Sample	Pt(0)			PtO _x		
	4f _{7/2} peak position/ eV	4f _{5/2} peak position/ eV	Percentage/ %	4f _{7/2} peak position/ eV	4f _{5/2} peak position/ eV	Percentage / %
Pt/CB	70.8	74.2	73.9	72.1	75.4	26.1
Pt/NCB-1	70.8	74.1	71.2	72.2	75.5	28.8
Pt/NCB-2	70.7	74.1	69.1	72.2	75.5	30.9
Pt/NCB-10	70.7	74.0	62.2	72.1	75.5	37.8

0.5 M H₂SO₄ at a scan rate of 50 mV s⁻¹. The prominent peaks appearing between 0.8 and 1.0 V were related to the CO stripping process, which can be employed to estimate the ECSA values based on the following formula [66]:

$$\text{ECSA} = \frac{Q_{\text{CO}}}{m_{\text{Pt}} \times 0.42}$$

Table 2 listed the detailed electrochemical results of all the studied catalysts. Among them, the Pt/NCB-

10 possesses the largest ECSA value of up to 76.3 m² g⁻¹, which is much higher than those of Pt/NCB-2 (74.1 m² g⁻¹), Pt/NCB-1 (65.3 m² g⁻¹), and Pt/CB (62.3 m² g⁻¹) catalysts. Furthermore, the N₂ adsorption–desorption analysis unravels a high Brunauer–Emmett–Teller (BET) surface area of 116.7 m² g⁻¹ for the Pt/NCB-10 architecture (Figure S9), which is comparable to the ECSA analysis. These results might arise from the high dispersion of small-sized Pt nanoparticles on NCB-10, thus leading to an

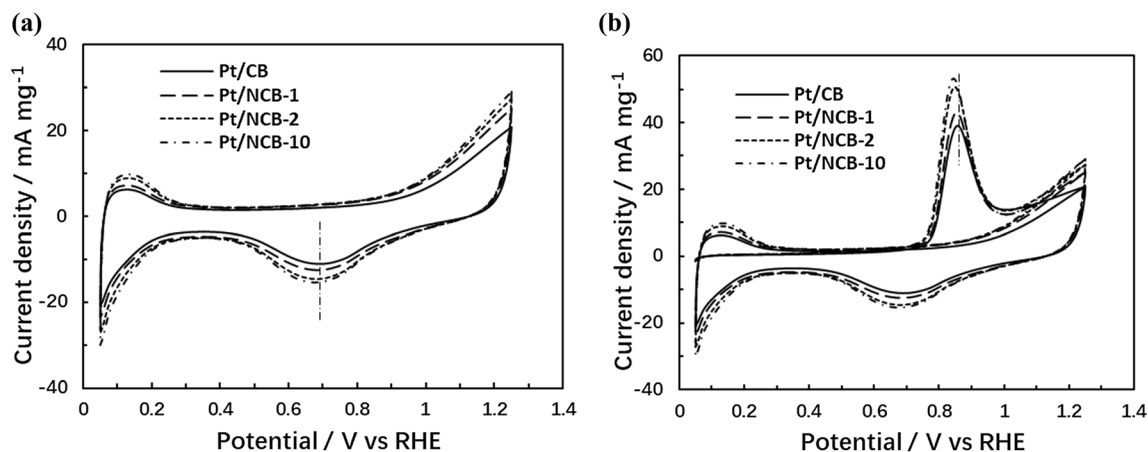


Figure 5 **a** CV curves and **b** CO-stripping voltammograms of the Pt/CB, Pt/NCB-1, Pt/NCB-2, and Pt/NCB-10 catalysts recorded in 0.5 M H₂SO₄ solution at the scan rate of 50 mV s⁻¹.

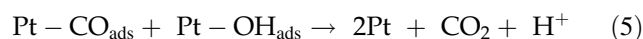
Table 2 A compiled study comparing CV results for Pt/NCB catalysts

	ECSA m ² g ⁻¹	0.5 M H ₂ SO ₄ + 1 M CH ₃ OH				1 M NaOH + 1 M CH ₃ OH			
		I _F A mg ⁻¹	I _R A m g ⁻¹	I _F /I _R	I _F /ECSA A m ⁻²	I _F A mg ⁻¹	I _R A mg ⁻¹	I _F /I _R	I _F /ECSA A m ⁻²
Pt/CB	62.3	0.331	0.325	1.03	5.31	1.49	0.43	3.47	23.92
Pt/NCB-1	65.3	0.387	0.331	1.17	5.93	1.83	0.4	4.58	28.02
Pt/NCB-2	74.1	0.506	0.343	1.47	6.83	2.74	0.46	5.96	36.98
Pt/NCB-10	76.3	0.593	0.362	1.63	7.78	3.02	0.42	7.19	39.58

enormous amount of accessible catalytically active sites on the electrode surface.

Figure 6a demonstrated the methanol electrooxidation curves of the four different catalysts. As expected, the Pt/NCB-10 manifested the highest activity of 0.593 A mg⁻¹ and the lowest potential monitored at a constant current, indicating that methanol oxidation reaction was more easily driven by Pt/NCB-10. As a reference, the Pt nanoparticles supported on NGQDs were also prepared and their catalytic performance as listed in Figure S10 and Table S2. The Pt/NGQDs deliver a low activity of 0.224 A mg⁻¹, which probably results from the relatively low electrical conductivity of NQGDs materials owing to the intrinsic plentiful oxygen-containing groups. The catalytic reaction of methanol on Pt can be considered into two processes. The first process is the gradual dehydrogenation of methanol molecules to form carbon-containing intermediates (-CO_{ads}), accumulated on the catalytic sites, which behaves the forward sweep peak (~ 0.85 V) in CV profiles [26]; subsequently, the -CO_{ads} intermediates are further oxidized to CO₂ by the presence of neighboring

adsorbed -OH_{ads}, corresponding the reverse sweep peak (~ 0.65 V), as shown in the following reaction equation [40, 67–69].



The forward sweep peak current density usually can be used to evaluate the catalytic activity of a catalyst for methanol electrooxidation, whereas the ratio of peak current in the forward scan (I_F) to the reverse scan (I_R) can describe the catalyst tolerance to the -CO_{ads} intermediates. [70] As can be seen in Table 2, the I_F/I_R ratio of the Pt/NCB-10 is found to be 1.63, superior to that of Pt/NCB-2 (1.47), Pt/NCB-1 (1.17), and Pt/CB (1.03), implying the involved nitrogen components from NGQDs might accelerate the adsorption of -OH_{ads}, [39] thus manage effectively removal of the -CO_{ads} intermediates, and generate

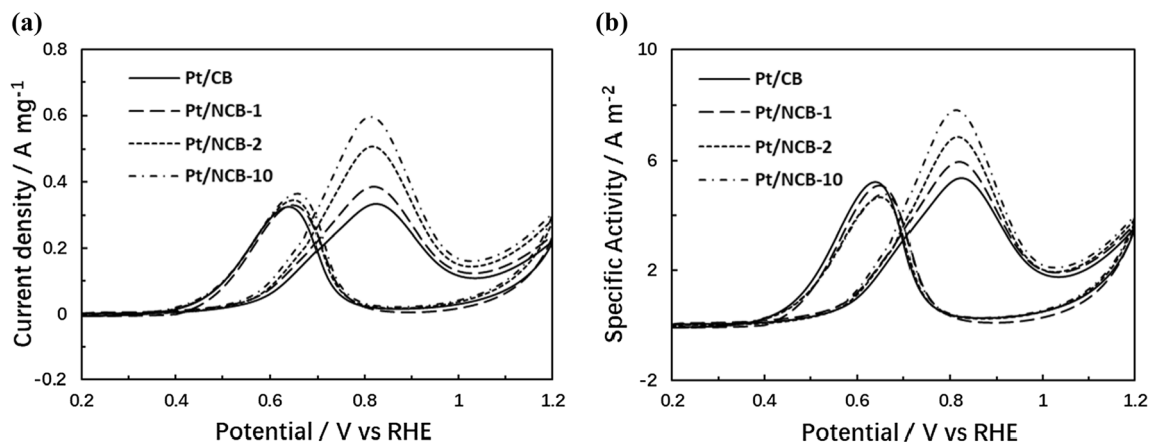


Figure 6 **a** Representative CV curves and **b** ECSA-averaged CV current densities of the Pt/CB, Pt/NCB-1, Pt/NCB-2, and Pt/NCB-10 catalysts recorded in 0.5 M H₂SO₄ with 1 M CH₃OH solution at the scan rate of 50 mV s⁻¹.

outstanding tolerance toward -CO_{ads} poisoning [71]. To gain further insight into the specific activities of these Pt catalysts, the electrochemical data has also been normalized to ECSA values. In Fig. 6b, the Pt/NCB-10 showed a 46% enhancement of the specific activity when compared with the commercially used Pt/CB catalyst. This gives distinct evidence that the pyridinic and pyrrolic N-enriched carbon support of NCB is crucial for increasing the catalytic activity per unit surface area of Pt. Such a phenomenon is related to the oxidation of the intermediate product of -CO_{ads} upon Pt/NCB-10, where pyridinic and pyrrolic N can active plentiful neighboring carbon atoms and accelerate the formation of -OH_{ads} by water dissociation (Eq. 5), thus releasing the catalytic active sites, increasing the utilization of the active sites, and strengthening the catalytic activity per active surface area. As a reference, we also prepared the N-doped carbon support using conventional thermal doping method, possessing a more graphitic N configuration. This N-doped carbon was then loaded with Pt nanoparticles, labeled with Pt/CB-N (Figure S11). The corresponding electrocatalytic performance toward methanol oxidation was presented in Figure S12, which unveiled a current density of 0.391 A mg⁻¹, higher than that of Pt/CB, demonstrating the strengthened metal-support interaction after integrating N components. However, compared with that of Pt/NCB-10, the enhancement is relatively low. Hence it's reasonable to conclude that the pyridinic and pyrrolic N possess a more significant impact on anchoring the metal particles, which is in agreement with the previous studies [51, 70].

The catalytic ability of the Pt/NCB-10 catalyst was also studied under various electrochemical conditions. Figure 7 presented the CVs obtained in the alkaline medium of 1 M NaOH with 1 M CH₃OH electrolyte at a scan rate of 50 mV s⁻¹. The CV curves for each catalyst had an oxidation peak in the forward and reverse scan portions similar to the acidic conditions, representing the direct oxidation of methanol on the catalyst surface and the oxidation of the residual adsorbed carbonaceous intermediates, respectively. Apparently, the electrochemical behaviors are kept almost unchanged, where the Pt/NCB-10 maintained the highest activity with an I_F value of 3.02 A mg⁻¹ as well as the most competitive I_F/I_R ratio among the four catalysts in this study. Thanks to the synergistic effect of nitrogen components on the support and Pt nanoparticles, the activities normalized to the ECSA values of these catalysts linearly with the nitrogen contents, in the order of Pt/CB < Pt/NCB-1 < Pt/NCB-2 < Pt/NCB-10, further demonstrating that surface nitrogen doping can effectively improve the electrocatalytic activity of Pt catalysts.

Other key requirements for the practical usage of the catalysts are long-term stability and durability. We then carried out typical i-t measurements of the Pt/CB, Pt/NCB-1, Pt/NCB-2, and Pt/NCB-10 catalysts in both acidic and alkaline media (Fig. 8). All of the catalysts experienced a sharp current decay at the initial stage, and subsequently a pseudo-steady-state gradually. This unavoidable decay most likely resulted from the accumulation of carbonaceous intermediates [72] that were generated during the

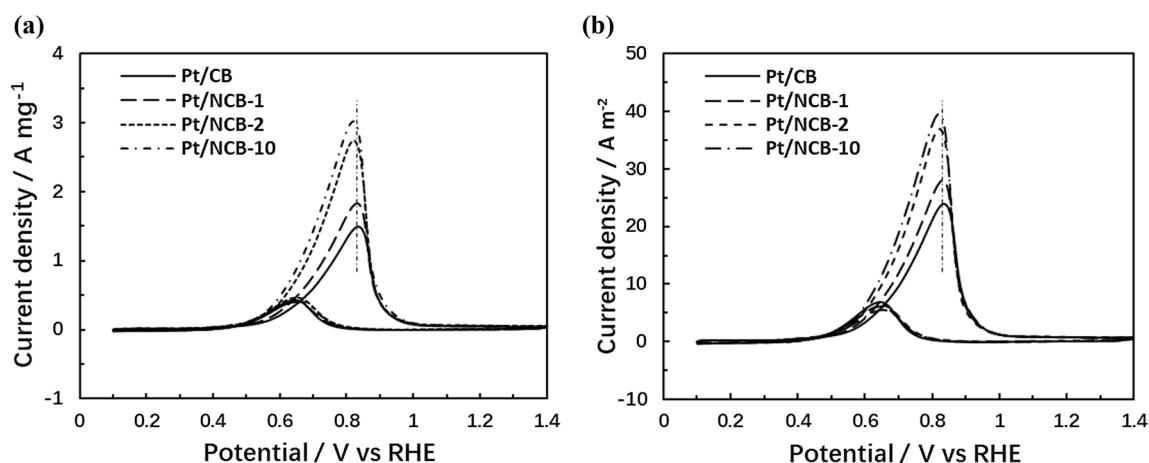


Figure 7 **a** Representative CV curves and **b** ECSA-averaged CV current densities of the Pt/CB, Pt/NCB-1, Pt/NCB-2, and Pt/NCB-10 catalysts recorded in 1 M NaOH with 1 M CH₃OH solution at the scan rate of 50 mV s⁻¹.

methanol oxidation, as listed in Eq. 1–4. These poisoning species occupied the Pt active sites and were then removed via the reaction of the neighbor dissociated $-\text{OH}_{\text{ads}}$ (Eq. 5). In comparison to those for Pt/CB, Pt/NCB-1, and Pt/NCB-2 the selected Pt/NCB-10 catalyst displayed a remarkably higher initial current and a slower decay rate, suggesting a far outstanding catalytic durability. Importantly, the durability of Pt/NCB-*n* shared the same tendency as the nitrogen contents, giving another proof of the effect of the nitrogen incorporation as well as the concerted effects of the individual components. Furthermore, Figure S13 showed the TEM images of the Pt/CB and Pt/NCB-10 catalysts subjected to the

durability test, where it can be clearly seen that the Pt/NCB-10 preserved highly dispersive Pt nanoparticles with an average size of 2.20 nm. In contrast, the Pt/CB exhibits a significantly enlarged size distribution and several aggregations. Such a phenomenon can be assigned to the Ostwald ripening during the harsh electrochemical catalysis process, which also verified that the strong metal–support link induced by the N component is able to stabilize the Pt nanoparticles more firmly to improve their structural stability.

The intriguing electrocatalytic properties of the Pt/NCB-*n* composites with synergistic structural features are mainly credited to the accompanying

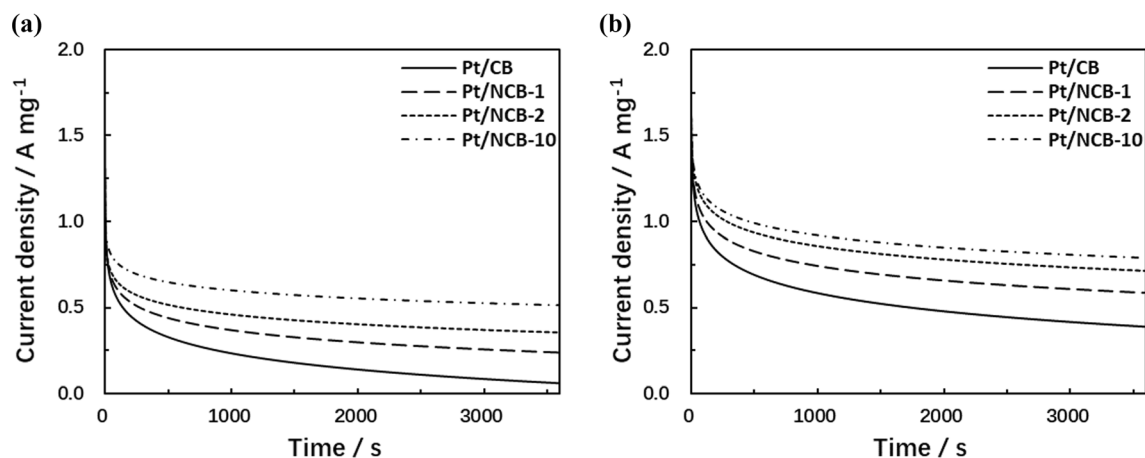


Figure 8 Typical *i*-*t* curves of the Pt/CB, Pt/NCB-1, Pt/NCB-2, and Pt/NCB-10 catalysts in (a) 0.5 M H₂SO₄ with 1 M CH₃OH solution at 0.40 V and (b) 1 M NaOH with 1 M CH₃OH solution at 0.70 V.

aspects: (i) the uniform dispersion of small-sized Pt nanoparticles on NCB-*n* delivers a narrow size distribution, which not only exerts large electrochemically accessible active sites and offers sufficient triple-phase boundaries but also fully exploits the catalytic functions and ensures fast electrocatalytic kinetics for methanol oxidation; (ii) the capital conservation of the intrinsically electronic structure of carbon support guarantees a rapid charge-transfer rate in this composite system, significantly promoting the electron diffusion in the methanol oxidation reactions; (iii) the chemically integrated nitrogen components possess a high proportion of active pyridinic and pyrrolic N, effectively anchoring and stabilizing the Pt nanoparticles via their strong interactions [73]. Combining the narrow Pt size distribution, it efficiently suppresses the Ostwald ripening effect upon the electrochemical catalysis process, thus greatly improving the structural stability of the catalyst. Moreover, the pyridinic and pyrrolic N energetically reduce the potential for producing -OH_{ads} species, simultaneously facilitating the elimination of the adsorbed poisoning intermediates, remarkably strengthening the poison tolerance ability.

Conclusions

In summary, we have demonstrated a convenient and scalable approach to chemically integrating nitrogen components upon the carbon support, giving typically over 90 at% proportion of highly active pyridinic and pyrrolic N configurations. The novel structural features serve as an ideal platform achieving stabilizing Pt nanoparticles with a small size of ~ 2 nm alongside narrow size distribution. Towards methanol oxidation, the resulting Pt/NCB-*n* possesses outstanding electrocatalytic performances, in particular, the Pt/NCB-10 presents a large ECSA value of $76.3 \text{ m}^2 \text{ g}^{-1}$, ultrahigh forward peak current densities (0.593 A mg^{-1} in acid media and 3.02 A mg^{-1} in alkaline media) as well as unusual poison tolerances and reliable long-term durability, which is significantly outperformed the commercial used Pt/CB catalysts. This great enhancement can be attributed to the unique nanostructure of Pt/NCB-*n*, sufficient accessible catalytically active sites, acceptable unimpeded electron transfer channels as well as strengthened strong catalyst-support interactions.

Acknowledgements

This work was supported by the National Natural Science Foundation of China (Grant Nos. 51772156 and 51872144).

Supplementary Information: The online version contains supplementary material available at <http://doi.org/10.1007/s10853-021-06856-4>.

References

- [1] Seh ZW, Kibsgaard J, Dickens CF, Chorkendorff I, Nørskov JK, Jaramillo TF (2017) Combining theory and experiment in electrocatalysis: insights into materials design. *Science* 355:eaad4998. <https://doi.org/10.1126/science.aad4998>
- [2] Chu S, Majumdar A (2012) Opportunities and challenges for a sustainable energy future. *Nature* 488:294. <https://doi.org/10.1038/nature11475>
- [3] Wu HB, Lou XWD (2017) Metal-organic frameworks and their derived materials for electrochemical energy storage and conversion: promises and challenges. *Sci Adv* 3:eaap9252. <https://doi.org/10.1126/sciadv.aap9252>
- [4] Debe MK (2012) Electrocatalyst approaches and challenges for automotive fuel cells. *Nature* 486:43. <https://doi.org/10.1038/nature11115>
- [5] Xiong Y, Dong J, Huang Z-Q et al (2020) Single-atom Rh/N-doped carbon electrocatalyst for formic acid oxidation. *Nat Nanotech* 15:390. <https://doi.org/10.1038/s41565-020-0665-x>
- [6] Zhang J, Zhao Z, Xia Z, Dai L (2015) A metal-free bifunctional electrocatalyst for oxygen reduction and oxygen evolution reactions. *Nat Nanotech* 10:444. <https://doi.org/10.1038/NNANO.2015.48>
- [7] Wang H, Xu S, Tsai C et al (2016) Direct and continuous strain control of catalysts with tunable battery electrode materials. *Science* 354:1031. <https://doi.org/10.1126/science.aaf7680>
- [8] Sun Y, Silvioli L, Sahraie NR et al (2019) Activity–selectivity trends in the electrochemical production of hydrogen peroxide over single-site metal–nitrogen–carbon catalysts. *J Am Chem Soc* 141:12372. <https://doi.org/10.1021/jacs.9b05576>
- [9] Wang J, Huang Z, Liu W et al (2017) Design of N-coordinated dual-metal sites: a stable and active Pt-free catalyst for acidic oxygen reduction reaction. *J Am Chem Soc* 139:17281. <https://doi.org/10.1021/jacs.7b10385>

- [10] Najam T, Shah SSA, Ding W et al (2018) An efficient anti-poisoning catalyst against SO_x, NO_x and PO_x: P, N-doped carbon for oxygen reduction in acidic media. *Angew Chem Int Ed* 57:15101. <https://doi.org/10.1002/anie.201808383>
- [11] Ge Y, Wang X, Huang B et al (2021) Seeded synthesis of unconventional 2H-phase Pd alloy nanomaterials for highly efficient oxygen reduction. *J Am Chem Soc* 143:17292. <https://doi.org/10.1021/jacs.1c08973>
- [12] Xie H, Chen S, Liang J et al (2021) Weakening intermediate bindings on CuPd/Pd core/shell nanoparticles to achieve Pt-like bifunctional activity for hydrogen evolution and oxygen reduction reactions. *Adv Funct Mater* 31:2100883. <https://doi.org/10.1002/adfm.202100883>
- [13] Xiao M, Zhu J, Li G et al (2019) A single-atom iridium heterogeneous catalyst in oxygen reduction reaction. *Angew Chem Int Ed* 58:9640. <https://doi.org/10.1002/ange.201905241>
- [14] Xiao M, Gao L, Wang Y et al (2019) Engineering energy level of metal center: Ru single-atom site for efficient and durable oxygen reduction catalysis. *J Am Chem Soc* 141:19800. <https://doi.org/10.1021/jacs.9b09234>
- [15] Gibbons BM, Wette M, Stevens MB et al (2020) In situ X-ray absorption spectroscopy disentangles the roles of copper and silver in a bimetallic catalyst for the oxygen reduction reaction. *Chem Mater* 32:1819. <https://doi.org/10.1021/acs.chemmater.9b03963>
- [16] Xiao M, Chen Y, Zhu J et al (2019) Climbing the apex of the ORR volcano plot via binuclear site construction: electronic and geometric engineering. *J Am Chem Soc* 141:17763. <https://doi.org/10.1021/jacs.9b08362>
- [17] Chen K, Liu K, An P et al (2020) Iron phthalocyanine with coordination induced electronic localization to boost oxygen reduction reaction. *Nat Commun* 11:1. <https://doi.org/10.1038/s41467-020-18062-y>
- [18] Chung HT, Cullen DA, Higgins D et al (2017) Direct atomic-level insight into the active sites of a high-performance PGM-free ORR catalyst. *Science* 357:479. <https://doi.org/10.1126/science.aan2255>
- [19] Yin P, Yao T, Wu Y et al (2016) Single cobalt atoms with precise N-coordination as superior oxygen reduction reaction catalysts. *Angew Chem Int Ed* 55:10800. <https://doi.org/10.1002/anie.201604802>
- [20] Aoki Y, Takase K, Kiuchi H et al (2021) In situ activation of a manganese perovskite oxygen reduction catalyst in concentrated alkaline media. *J Am Chem Soc* 143:6505. <https://doi.org/10.1021/jacs.1c00449>
- [21] Gonell F, Sánchez-Sánchez CM, Vivier V, Méthivier C, Laberty-Robert C, Portehault D (2020) Structure-activity relationship in manganese perovskite oxide nanocrystals from molten salts for efficient oxygen reduction reaction electrocatalysis. *Chem Mater* 32:4241. <https://doi.org/10.1021/acs.chemmater.0c00681>
- [22] Wang S, Zhang L, Xia Z et al (2012) BCN graphene as efficient metal-free electrocatalyst for the oxygen reduction reaction. *Angew Chem Int Ed* 51:4209. <https://doi.org/10.1002/anie.201109257>
- [23] Han Y, Wang Y-G, Chen W et al (2017) Hollow N-doped carbon spheres with isolated cobalt single atomic sites: superior electrocatalysts for oxygen reduction. *J Am Chem Soc* 139:17269. <https://doi.org/10.1021/jacs.7b10194>
- [24] Zhang X, Zhang S, Yang Y et al (2020) A general method for transition metal single atoms anchored on honeycomb-like nitrogen-doped carbon nanosheets. *Adv Mater* 32:1906905. <https://doi.org/10.1002/adma.201906905>
- [25] Liu L, Lopez-Haro M, Lopes CW et al (2019) Regioselective generation and reactivity control of subnanometric platinum clusters in zeolites for high-temperature catalysis. *Nature Mater* 18:866. <https://doi.org/10.1038/s41563-019-0412-6>
- [26] Kang Y, Pyo JB, Ye X, Gordon TR, Murray CB (2012) Synthesis, shape control, and methanol electro-oxidation properties of Pt–Zn alloy and Pt₃Zn intermetallic nanocrystals. *ACS Nano* 6:5642. <https://doi.org/10.1021/nl301583g>
- [27] Huang L, Zhang X, Wang Q, Han Y, Fang Y, Dong S (2018) Shape-control of Pt–Ru nanocrystals: tuning surface structure for enhanced electrocatalytic methanol oxidation. *J Am Chem Soc* 140:1142. <https://doi.org/10.1021/jacs.7b12353>
- [28] Huang X, Zhang H, Guo C, Zhou Z, Zheng N (2009) Simplifying the creation of hollow metallic nanostructures: one-pot synthesis of hollow palladium/platinum single-crystalline nanocubes. *Angew Chem Int Ed Engl* 48:4808. <https://doi.org/10.1002/anie.200900199>
- [29] Cui C, Gan L, Neumann M, Heggen M, Cuenya BR, Strasser P (2014) Carbon monoxide-assisted size confinement of bimetallic alloy nanoparticles. *J Am Chem Soc* 136:4813. <https://doi.org/10.1021/ja4124658>
- [30] Cui Z, Chen H, Zhao M et al (2014) Synthesis of structurally ordered Pt₃Ti and Pt₃V nanoparticles as methanol oxidation catalysts. *J Am Chem Soc* 136:10206. <https://doi.org/10.1021/ja504573a>
- [31] Saleem F, Zhang Z, Xu B, Xu X, He P, Wang X (2013) Ultrathin Pt–Cu nanosheets and nanocones. *J Am Chem Soc* 135:18304. <https://doi.org/10.1021/ja4101968>
- [32] Vinayan BP, Nagar R, Rajalakshmi N, Ramaprabhu S (2012) Novel platinum-cobalt alloy nanoparticles dispersed on nitrogen-doped graphene as a cathode electrocatalyst for PEMFC applications. *Adv Funct Mater* 22:3519. <https://doi.org/10.1002/adfm.201102544>
- [33] Uhm S, Lee HJ, Kwon Y, Lee J (2008) A stable and cost-effective anode catalyst structure for formic acid fuel cells.

- Angew Chem 120:10317. <https://doi.org/10.1002/anie.200803466>
- [34] Kuttiyiel KA, Sasaki K, Choi Y, Su D, Liu P, Adzic RR (2012) Nitride stabilized PtNi core-shell nanocatalyst for high oxygen reduction activity. *Nano Lett* 12:6266. <https://doi.org/10.1021/nl303362s>
- [35] Xie J, Zhang Q, Gu L et al (2016) Ruthenium–platinum core–shell nanocatalysts with substantially enhanced activity and durability towards methanol oxidation. *Nano Energy* 21:247. <https://doi.org/10.1016/j.nanoen.2016.01.013>
- [36] Wang D, Xin HL, Hovden R et al (2013) Structurally ordered intermetallic platinum–cobalt core–shell nanoparticles with enhanced activity and stability as oxygen reduction electrocatalysts. *Nat Mater* 12:81. <https://doi.org/10.1038/NMAT3458>
- [37] Meng C, Ling T, Ma TY et al (2017) Atomically and electronically coupled Pt and CoO hybrid nanocatalysts for enhanced electrocatalytic performance. *Adv Mater* 29:1604607. <https://doi.org/10.1002/adma.201604607>
- [38] Chang J, Feng L, Liu C, Xing W, Hu X (2014) Ni₂P enhances the activity and durability of the Pt anode catalyst in direct methanol fuel cells. *Energy Environ Sci* 7:1628. <https://doi.org/10.1039/c4ee00100a>
- [39] Zhou Y, Neyerlin K, Olson TS et al (2010) Enhancement of Pt and Pt-alloy fuel cell catalyst activity and durability via nitrogen-modified carbon supports. *Energy Environ Sci* 3:1437. <https://doi.org/10.1039/c003710a>
- [40] Zhang W, Yao Q, Jiang G et al (2019) Molecular trapping strategy to stabilize subnanometric Pt clusters for highly active electrocatalysis. *ACS Catal* 9:11603. <https://doi.org/10.1021/acscatal.9b02987>
- [41] Shen R, Chen W, Peng Q et al (2019) High-concentration single atomic Pt sites on hollow CuS_x for selective O₂ reduction to H₂O₂ in acid solution. *Chem* 5:2099. <https://doi.org/10.1016/j.chempr.2019.04.024>
- [42] Karuppanan M, Kim Y, Gok S et al (2019) A highly durable carbon-nanofiber-supported Pt–C core–shell cathode catalyst for ultra-low Pt loading proton exchange membrane fuel cells: facile carbon encapsulation. *Energy Environ Sci* 12:2820. <https://doi.org/10.1039/C9EE01000A>
- [43] Lai WH, Zhang BW, Hu Z et al (2019) The Quasi-Pt-alloy catalyst: hollow PtCo@ single-atom PtI on nitrogen-doped carbon toward superior oxygen reduction. *Adv Funct Mater* 29:1807340. <https://doi.org/10.1002/adfm.201807340>
- [44] Hu C, Dai L (2019) Doping of carbon materials for metal-free electrocatalysis. *Adv Mater* 31:1804672. <https://doi.org/10.1002/adma.201804672>
- [45] Jia Y, Zhang L, Zhuang L et al (2019) Identification of active sites for acidic oxygen reduction on carbon catalysts with and without nitrogen doping. *Nat Catal* 2:688. <https://doi.org/10.1038/s41929-019-0297-4>
- [46] Paul R, Du F, Dai L et al (2019) 3D heteroatom-doped carbon nanomaterials as multifunctional metal-free catalysts for integrated energy devices. *Adv Mater* 31:1805598. <https://doi.org/10.1002/adma.201805598>
- [47] Zhang W, Huang H, Li F, Deng K, Wang X (2014) Palladium nanoparticles supported on graphitic carbon nitride-modified reduced graphene oxide as highly efficient catalysts for formic acid and methanol electrooxidation. *J Mater Chem A* 2:19084. <https://doi.org/10.1039/c4ta03326d>
- [48] Zheng Y, Jiao Y, Zhu Y et al (2017) Molecule-level g-C₃N₄ coordinated transition metals as a new class of electrocatalysts for oxygen electrode reactions. *J Am Chem Soc* 139:3336. <https://doi.org/10.1021/jacs.6b13100>
- [49] Jiao Y, Zheng Y, Chen P, Jaroniec M, Qiao S-Z (2017) Molecular scaffolding strategy with synergistic active centers to facilitate electrocatalytic CO₂ reduction to hydrocarbon/alcohol. *J Am Chem Soc* 139:18093. <https://doi.org/10.1021/jacs.7b10817>
- [50] Zhang W, Peng Q, Shi L et al (2019) Merging single-atom-dispersed iron and graphitic carbon nitride to a joint electronic system for high-efficiency photocatalytic hydrogen evolution. *Small* 15:1905166. <https://doi.org/10.1002/sml.201905166>
- [51] Huang H, Ma L, Tiwary CS et al (2017) Worm-shape Pt nanocrystals grown on nitrogen-doped low-defect graphene sheets: highly efficient electrocatalysts for methanol oxidation reaction. *Small* 13:1603013. <https://doi.org/10.1002/sml.201603013>
- [52] Krishnamoorthy K, Veerapandian M, Yun K, Kim S-J (2013) The chemical and structural analysis of graphene oxide with different degrees of oxidation. *Carbon* 53:38. <https://doi.org/10.1016/j.carbon.2012.10.013>
- [53] Marcano DC, Kosynkin DV, Berlin JM et al (2010) Improved synthesis of graphene oxide. *ACS Nano* 4:4806. <https://doi.org/10.1021/nn1006368>
- [54] Xu C, Wang X, Zhu J (2008) Graphene–metal particle nanocomposites. *J Phys Chem C* 112:19841. <https://doi.org/10.1021/jp807989b>
- [55] Wang S, Chen Z-G, Cole I, Li Q (2015) Structural evolution of graphene quantum dots during thermal decomposition of citric acid and the corresponding photoluminescence. *Carbon* 82:304. <https://doi.org/10.1016/j.carbon.2014.10.075>
- [56] Dong Y, Shao J, Chen C et al (2012) Blue luminescent graphene quantum dots and graphene oxide prepared by tuning the carbonization degree of citric acid. *Carbon* 50:4738. <https://doi.org/10.1016/j.carbon.2012.06.002>
- [57] Zhang W, Zhang M, Liu W, Yu A (2021) Molten-based defect engineering polymeric carbon nitride quantum dots

- with enhanced hole extraction: an efficient photoelectrochemical cell for water oxidation. *Carbon* 173:339. <https://doi.org/10.1016/j.carbon.2020.11.032>
- [58] Borse V, Thakur M, Sengupta S, Srivastava R (2017) N-doped multi-fluorescent carbon dots for ‘turn off-on’ silver-biothiol dual sensing and mammalian cell imaging application. *Sens Actuators B Chem* 248:481. <https://doi.org/10.1016/j.snb.2017.03.158>
- [59] Gong X, Li Z, Hu Q, Zhou R, Shuang S, Dong C (2017) N, S, P Co-doped carbon nanodot fabricated from waste microorganism and its application for label-free recognition of manganese (VII) and L-ascorbic acid and AND logic gate operation. *ACS Appl Mater Interfaces* 9:38761. <https://doi.org/10.1021/acsami.7b11170>
- [60] Li D, Müller MB, Gilje S, Kaner RB, Wallace GG (2008) Processable aqueous dispersions of graphene nanosheets. *Nature Nanotech* 3:101. <https://doi.org/10.1038/nnano.2007.451>
- [61] Dong Y, Pang H, Yang HB et al (2013) Carbon-based dots co-doped with nitrogen and sulfur for high quantum yield and excitation-independent emission. *Angew Chem Int Ed* 52:7800. <https://doi.org/10.1002/anie.201301114>
- [62] Lim SY, Shen W, Gao Z (2015) Carbon quantum dots and their applications. *Chem Soc Rev* 44:362. <https://doi.org/10.1039/c4cs00269e>
- [63] Li H, He X, Kang Z et al (2010) Water-soluble fluorescent carbon quantum dots and photocatalyst design. *Angew Chem* 122:4532. <https://doi.org/10.1002/anie.200906154>
- [64] Huang H, Zhu J, Zhang W et al (2016) Controllable codoping of nitrogen and sulfur in graphene for highly efficient Li-oxygen batteries and direct methanol fuel cells. *Chem Mater* 28:1737. <https://doi.org/10.1021/acs.chemmater.5b04654>
- [65] Tang K, Wang X, Li Q, Yan C (2018) High edge selectivity of in situ electrochemical Pt deposition on edge-rich layered WS₂ nanosheets. *Adv Mater* 30:1704779. <https://doi.org/10.1002/adma.201704779>
- [66] Zhang W, Yao Q, Wu X, Fu Y, Deng K, Wang X (2016) Intimately coupled hybrid of graphitic carbon nitride nanoflakelets with reduced graphene oxide for supporting Pd nanoparticles: a stable nanocatalyst with high catalytic activity towards formic acid and methanol electrooxidation. *Electrochim Acta* 200:131. <https://doi.org/10.1016/j.electacta.2016.03.169>
- [67] Zhang W, Fu Y, Wang J, Wang X (2017) 3D Hierarchically porous graphitic carbon nitride modified graphene-Pt hybrid as efficient methanol oxidation catalysts. *Adv Mater Interfaces* 4:1601219. <https://doi.org/10.1002/admi.201601219>
- [68] Greeley J, Mavrikakis M (2004) Competitive paths for methanol decomposition on Pt (111). *J Am Chem Soc* 126:3910. <https://doi.org/10.1021/ja037700z>
- [69] Feng Q, Zhao S, He D et al (2018) Strain engineering to enhance the electrooxidation performance of atomic-layer Pt on intermetallic Pt₃Ga. *J Am Chem Soc* 140:2773. <https://doi.org/10.1021/jacs.7b13612>
- [70] Huang H, Yang S, Vajtai R, Wang X, Ajayan PM (2014) Pt-decorated 3D architectures built from graphene and graphitic carbon nitride nanosheets as efficient methanol oxidation catalysts. *Adv Mater* 26:5160. <https://doi.org/10.1002/adma.201401877>
- [71] Zhang S, Wang H, Zhang N, Kong F, Liu H, Yin G (2012) Role of Pt-pyridinic nitrogen sites in methanol oxidation on Pt/polypyrrole-carbon black catalyst. *J Power Sources* 197:44. <https://doi.org/10.1016/j.jpowsour.2011.09.031>
- [72] Wang C, Yue R, Wang H et al (2014) Dendritic Ag@ Pt core-shell catalyst modified with reduced graphene oxide and titanium dioxide: fabrication, characterization, and its photo-electrocatalytic performance. *Int J Hydrogen Energy* 39:5764. <https://doi.org/10.1016/j.ijhydene.2014.01.192>
- [73] Zhang Z, Chen Y, Zhou L et al (2019) The simplest construction of single-site catalysts by the synergism of micropore trapping and nitrogen anchoring. *Nat Commun* 10:1. <https://doi.org/10.1038/s41467-019-09596-x>

Publisher's Note Springer Nature remains neutral with regard to jurisdictional claims in published maps and institutional affiliations.